Quantum dots: promises and accomplishments

Exploration of the Stranski-Krastanow growth of strained semiconductor heterostructures marked the major breakthrough for easy fabrication of defect-free quantum dots (QDs). For the first time, single QDs are facilitating the development of electrically operated emitters of single polarized or entangled photons on demand: an essential component for quantum communication systems. QDs inserted in quantum wells, stacked in planes upon each other, have led to semiconductor lasers that can operate at wavelengths that were previously impossible, or at least difficult to reach, for a given semiconductor family. These lasers show excellent temperature stability, large radiation resistance, and excellent temporal and spatial stability. In this review we discuss recent progress in the field of quantum dot devices.

Dieter Bimberg* and Udo W. Pohl

Institut für Festkörperphysik, Technische Universität Berlin, 10623 Berlin, Germany

**E-mail: bimberg@physik.tu-berlin.de*

The electronic density of states (DOS) of charge carriers in a semiconductor is significantly modified if the wave function is spatially confined. In the ultimate limit of three-dimensional (3D) charge carrier confinement the energy levels are quantized in all spatial directions and the energy levels are discrete. For typical spatial dimensions of ~10 nm the energy separation of the levels is in the range of 10 – 100 meV, depending on the effective carrier mass. The discrete energy spectrum of such a single quantum dot resembles that of an atom embedded in a dielectric matrix provided by a confining semiconductor with a larger band gap[1].

In the 1970s Dingle and Henry recognized that energy quantization in quantum wells could be exploited for semiconductor lasers to lower the lasing threshold and to provide a tunable wavelength[2]. Size quantization leads to an increase of the DOS near the band edge in QWs (Fig. 1a). When the dimensionality of the active layer is further reduced, injected charge carriers concentrate in an increasingly narrow energy range near the band edge. Consequently the maximum material gain increases and the temperature dependence of laser parameters is reduced. These effects were predicted theoretically in the 80s by Asada *et al*. and Arakawa and Sakaki for lattice-matched heterostructures like GaAs/AlGaAs[3,4]. By considering dots with a cubic shape, containing just one confined electron and hole state, a gain increase of an order of magnitude and a corresponding reduction of the threshold current was predicted, along with an increase of temperature stability. The final point is a beautiful illustration of the impact of a discrete DOS. While in bulk materials charge carriers are

ISSN:1369 7021 © Elsevier Ltd 2011

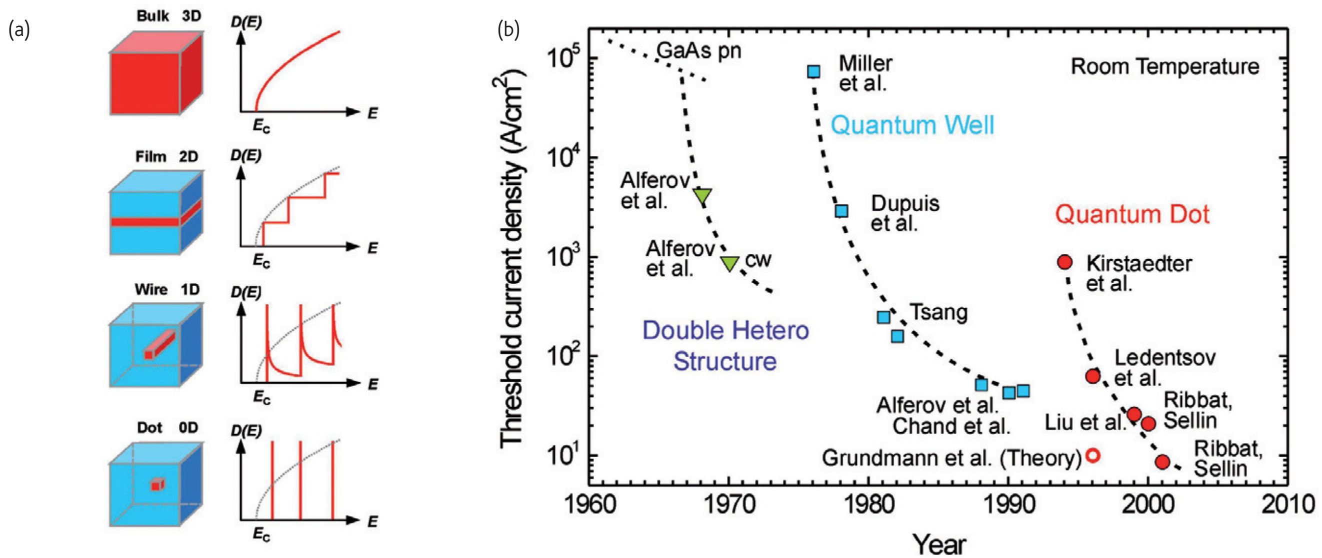

Fig. 1 Effect of reduced dimensionality. (a) Charge carriers are confined in a semiconductor (red) with a smaller bandgap than the cladding semiconductor (blue). The confinement changes the density of states D(E). E_C is the conduction-band edge of a 3D semiconductor. (b) Development of the threshold current-density of heterostructure lasers. A marked decrease of threshold was accomplished by introducing structures with reduced dimensionality: quantum wells and quantum dots.

continuously distributed to higher energy states as the temperature is raised, no such redistribution can occur in zero-dimensional structures, if the excited states lie sufficiently above the ground state. All carriers then contribute to the inversion at lasing energy, independent of temperature.

It took almost another decade for the authors' group to experimentally demonstrate the first realistic quantum dot lasers with superior properties. These were not based on lattice matched heterostructures, but on strongly strained ones. This breakthrough succeeded when the self-organized growth of dense arrays of coherent quantum dots, overgrown with large band-gap barrier material, based on strained-layer heteroepitaxy was developed. The first quantum-dot laser produced using this approach confirmed the predicted ultralow threshold current density (120 A/cm^2) and its low temperature dependence (T_0 = 350 K) at 77 K[5]. The following years showed rapid improvements in the performance of quantum-dot lasers, as evidenced by the threshold current data (Fig. 1b)[6], and at the beginning of the new millennium quantum-dot lasers were introduced to the market[7].

The original predictions of superior performance of quantum-dot lasers[3] were based on assumptions, which were later observed not to apply. Real quantum dots usually have several excited states which may be thermally occupied. Stranski-Krastanow growth leads, moreover, to the formation of a wetting layer of quantum-dot material underneath the dots, influencing carrier capture and reemission processes and thus the dynamics of lasers. Self-organized growth induces some variation of the size and shape of the dots, leading to a spread of localization energy within a dot ensemble. The lineshape of the ensemble luminescence, which is composed of a superposition of numerous Lorentzian single-dot lineshapes, is then inhomogeneously broadened (typically ≥ 50 meV). Thus the carrier distribution function of a real dot ensemble progressively changes from a nonthermal distribution to a Fermi function at high temperatures (typically ≥ 300 K), also found for the bulk material[8] if the barriers are not too high.

Device applications based on quantum dots may either involve a very large number of dots in an ensemble, or few dots, or individual dots. We first focus on applications requiring a large density of dots.

Devices employing ensembles of quantum dots

Self-organized growth easily yields a high density of mid 10^{10} cm^{-2} quantum dots in a single layer. Most prominent applications of dense ensembles of quantum dots are near-infrared lasers treated in more detail in the following, even though QDs are also attractive for improving other devices such as, e.g., solar cells: QDs were employed to realise the concept of intermediate-band solar cells[9], where the partially occupied intermediate band of the confined QD levels results in additional sub-bandgap absorption in a single-junction cell[10]. The proof of concept has been demonstrated, and progress in this interesting field is encouraging[11].

In laser applications a high dot density results in a large material gain[12], since the optical gain is proportional to the number of inverted states involved. Two types of lasers presently dominate the market: edge-emitting lasers and surface-emitting lasers. We first focus on lasers with edge-emitting geometry.

Using quantum dots for the active area of in edge-emitting lasers and optical amplifiers offers a number of decisive advantages. Tuning ability of the emission wavelength by control of their size and composition allows operation in the important datacom

O-band (1.26 – 1.36 µm) for GaAs-based devices. The carrier confinement in the dots efficiently suppresses carrier diffusion. This leads to an excellent temporal and spatial stability of the near field of the transverse ground mode[13,14], suppressing filamentation and improving degradation resistance under high-energy particle radiation[15] as is present in space applications. QD lasers have also proved robust against optical feedback into the cavity[16], reducing high frequency noise. Furthermore, ultrafast population dynamics in QD-based gain media has been found[17,18], making such materials interesting for applications in saturable absorbers and optical amplifiers.

Mode-locked lasers

There is a significant demand for monolithic semiconductor mode-locked lasers (MLL) to generate high-frequency optical pulse trains as pulse sources for datacom, optical clocks in electronic circuits, optical sampling of high-speed signals, and metrology. The operation principle illustrated in Fig. 2a depicts how the laser cavity is formed by the outer facets of a ridge-waveguide structure, which is divided into a gain section and a reverse-biased absorber section. Pulse trains are produced by intensity-dependent absorption in the passive or modulated (® hybrid MLL) absorber. A fast absorber recovery is a crucial requirement for achieving a short pulse width[19] in mode-locked lasers. High-frequency pulses require short cavities for short roundtrip duration (e.g., 80 GHz was demonstrated for a passive 450 + 50 µm long QD device[20]), and hence high gain and fast recovery.

A small timing jitter within the optical pulse train is of particular importance for most applications. The ultrafast gain recovery and reduced feedback sensitivity of QD-based gain media promise a lower jitter than expected for QW-based devices. Excellent data of a hybrid mode-locked device are shown in Fig. 2b. A root-mean-square (rms) timing jitter as low as 190 fs is accomplished at 40 GHz operation[21]. The measurement shows that the jitter is reduced for increased reverse bias at the absorber section. The observed values are well below the ITU recommendations for 40 GHz sources that specify a root-mean-square timing jitter below 2.5 ps for the integration range 20 – 320 MHz[22]. Data transmission at 40 Gb/s by an external synchronized modulation of the laser pulse-train is illustrated in Fig. 2c (left) [23]. The 40 GHz pulse train also proved to be suitable for generating optical data streams at 160 Gb/s. Chirp compression was applied yielding pulses with 700 fs full width at half maximum (FWHM), a value near the theoretical limit. Fig 2c (right) shows a 160 GHz pulse comb formed by two-stage optical time-division multiplexing (OTDM) of the hybrid mode-locked QD laser[23].

Semiconductor optical amplifiers

Future optical networks generate a large need for low-cost linear amplifiers, switches, wavelength converters, and optical signal regenerators, stimulating R+D of semiconductor optical amplifiers (SOAs). Such devices consist of a ridge-waveguide structure with non-reflecting cavity facets (anti-reflection coated or/and tilted) to prevent

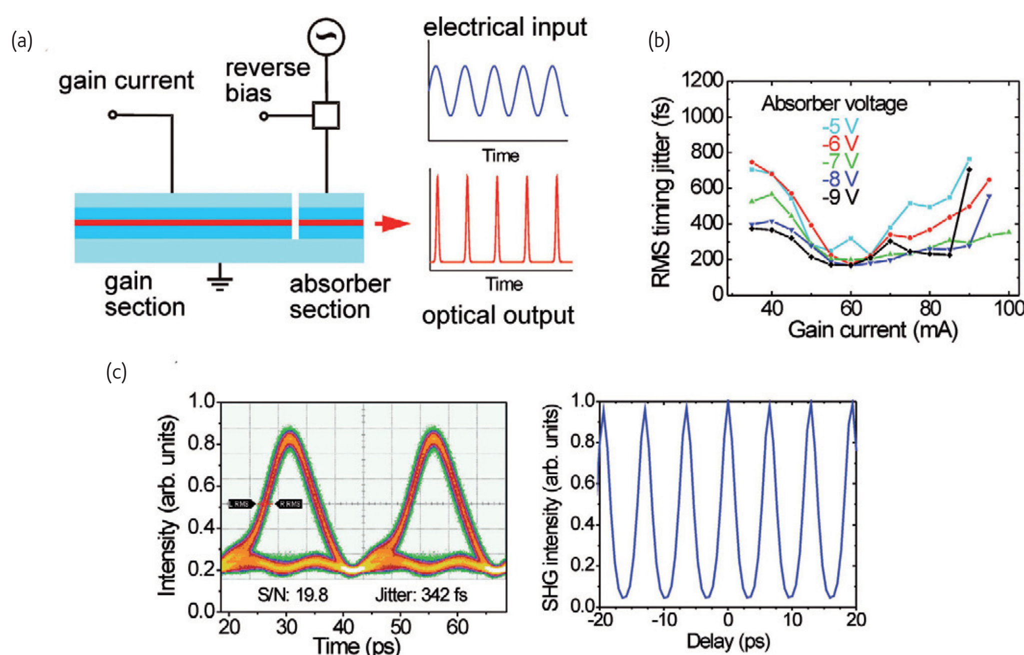

Fig. 2 (a) Schematic of a mode-locked laser with hybrid mode locking. The ridge-waveguide laser structure is divided into gain and absorber sections separated by a small air gap. The modulated absorption generates a synchronous optical pulse train (b) RMS timing jitter of a hybrid mode-locked QD laser operated at 40 GHz, derived from the single-side band noise integrated from 1 kHz to 1 GHz. (c) Left: Optical 40 Gb/s data stream generated from external modulation of the 40 GHz optical pulse train. Right: Autocorrelation measurement of the 40 GHz pulse train, upconverted to a pulse comb at 160 GHz by a two-stage optical-time-division multiplexing.

lasing as illustrated in the scheme Fig. 3a. The ultrafast gain recovery and broad bandwidth of QD gain media leads to large advantages as compared to QW and bulk media for any of the above applications.

Fig. 3a demonstrates wavelength conversion required for all-optical multi-wavelength networks. The conversion is accomplished using nonlinear cross-gain modulation (XGM). The SOA is deeply saturated by a large current. A modulated optical signal at λ_{red} leads to a modulation of the SOA gain. Consequently an additional weak continuous wave (CW) optical probe signal at λ_{blue} is affected by the gain modulation and leaves the SOA with a modulation inverted with respect to that of λ_{red}.

The cross-gain modulation bandwidth of a QD SOA is compared to that of a conventional QW SOA in Fig. 3b[24]. The 3 dB XGM bandwidth of the QW SOA is almost independent of the injection current and close to 15 GHz (30 GHz QW SOAs optimized for XGM[25]). In contrast, for increasing current QD SOAs show almost frequency-independent gain well beyond 40 GHz, much larger than the best ever reported values. The different dependence on injection current originates from the transition between two different gain saturation mechanisms in the QD SOA[26]. At frequencies below 10 GHz the carrier reservoir (basically the wetting-layer QW) follows the modulation caused by total carrier depletion. This mechanism also governs the QW SOA. Above 10 GHz spectral hole burning and its ultrafast recovery[27] becomes the dominant saturation process in the QD SOA and enables a large XGM bandwidth. Thus QD SOAs benefit from the dynamics of a QD ensemble.

Upconversion of a 80 Gb/s data stream at 1292 to 1300 nm using XGM of a QD SOA is demonstrated in Fig. 3c[28]. The eye diagram of the converted output signal is clearly open and shows low patterning effects. Recently[30] error-free XGM between 1310 and 1320 nm was shown at 80 Gb/s with a bit-error-rate below 10^{-9}. The data indicate the potential of XGM in GaAs-based QD SOAs for 100 Gb/s transmission at a single-wavelength channel. For InP-based QD SOAs open eyes were demonstrated for a 160 Gb/s data stream[31].

Vertical-cavity surface-emitting lasers

Semiconductor lasers with a vertical cavity offer a number of favorable properties. They produce a circular beam of high quality which is readily coupled to a fiber, operate at low threshold currents enabling high-speed modulation, feature a small temperature dependence up

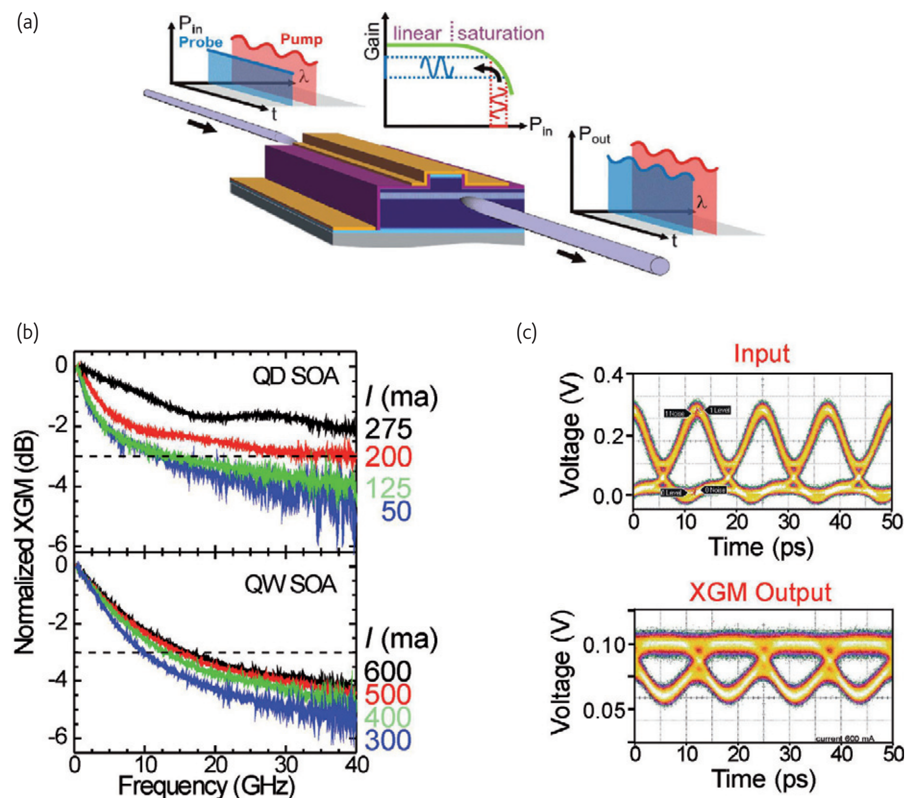

Fig. 3 Cross-gain modulation of a semiconductor optical amplifier (SOA). (a) Operation principle: a strong, modulated pump signal (P_{in}, red) drives the SOA into the saturation regime. Consequently the SOA gain is also modulated. The modulation pattern can be transferred to a weak CW probe pulse at another wavelength (P_{in}, blue), yielding an inverted modulation pattern on the probe signal in the output (P_{out}, blue). (b) Efficiency of the cross-gain modulation of a QD SOA (top) and a conventional QW SOA (bottom). The 3dB bandwidth of the QD SOA marked by the horizontal line can be tuned to beyond 40 GHz at high injection current. (c) Wavelength upconversion using cross-gain modulation of a QD SOA and a pseudorandom RZ-OOK- modulation. Top: input eye diagram of a 80 Gb/s signal at 1292 nm wavelength, bottom: upconverted output signal at 1300 nm.

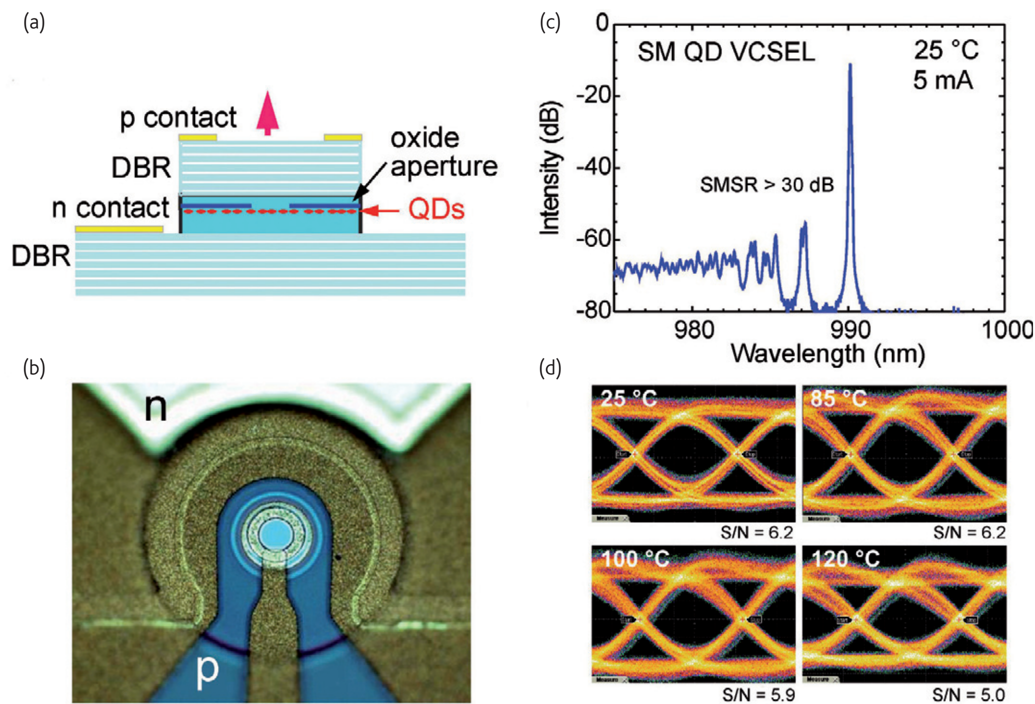

Fig. 4 A vertical-cavity surface-emitting laser (VCSEL). (a) Schematic view in cross section. The optically active medium comprising the quantum dots (QDs) is clad by two distributed-Bragg reflectors (DBR) forming an optical cavity. The radiation is vertically emitted (red arrow). (b) Top view of a typical device showing the aperture and the contacts. (c) Emission spectrum given on a logarithmic scale. (d) Eye diagrams showing 20 Gb/s operation of the device up to 120 °C for large-signal modulation. The open eyes demonstrate good signal-to-noise ratio also at high operation temperature.

to 85 °C, and more. Moreover, vertical-cavity surface-emitting lasers (VCSELs) are produced in a planar technology, which allows efficient on-chip testing at an early stage in the production process and vertical integration of components like modulators. The configuration of a VCSEL is shown in Fig. 4a. The active medium (QDs or QWs) is placed in a vertical cavity generally formed by distributed-Bragg-reflector mirrors. Low losses at each reflection are crucial, since the cavity is very short and the gain per cycle is low. The beam divergence is very low due to the large output aperture. A fully processed GaAs-based QD VCSEL is presented in Fig. 4b. The top-view micrograph shows the circular output aperture and the *p* and *n* contacts.

VCSELs based on GaAs/AlAs benefit from a larger refractive-index step and higher thermal conductivity compared to InP-based devices, and selective oxidation of AlAs to AlO_x allows for fabrication of buried oxide-confined apertures without complex overgrowth processes. Quantum-well VCSELs operating at 0.85 µm emission, the standard wavelength in the data communication industry, are an established product on the market today for optical computer mice, and considerable effort is presently being spent on replacing copper wires in high-speed short-range (< 300 m) data links using multi-mode optical fibers and such QW VCSELs. Today's commercial datacom QW VCSELs are designed for 10 Gb/s data rates. Recent developments achieved bandwidths larger than 20 GHz[32] and large signal error-free data rates (bit-error-rate below 10^{-12}) at 40 Gb/s[33] for this wavelength. Very recently an error-free data rate of 44 Gb/s was achieved for devices with strained QWs operating at 985 nm[34].

Application of quantum-dot gain media opens also the 1.3 µm datacom window for GaAs-based VCSELs. First QD VCSELs fabricated using MBE[35,36,37] or MOVPE[38] were presented already some time ago, and devices meanwhile attained a promising maturity. Recent advances were also achieved using sub-monolayer quantum dots instead of the Stranski-Krastanow quantum dots introduced above[39]. Such 0D structures are fabricated by deposition of a short-period superlattice of sub-monolayer thick InAs alternating with few monolayer-thick GaAs spacer material, leading to In-rich localization centers[40]. Error-free data transmission at 20 Gb/s was achieved for direct modulated devices operating at 980 nm up to 85 °C[38], and clearly open eyes at this data rate were demonstrated up to 120 °C[41].

Two innovative concepts of vertical emitters are presently emerging for the development of future optical interconnects: VCSELs with an implemented electro-optically modulator (EOM-VCSELs), and micro/nanolasers with a metal-coated cavity. For both approaches proofs-of-concepts were recently provided using quantum-well gain media.

EOM-VCSELs

An approach for realizing high-speed modulated VCSELs is the monolithic integration of a modulator into a VCSEL. The modulator is based on the quantum-confined Stark effect[42], which describes the shift of the

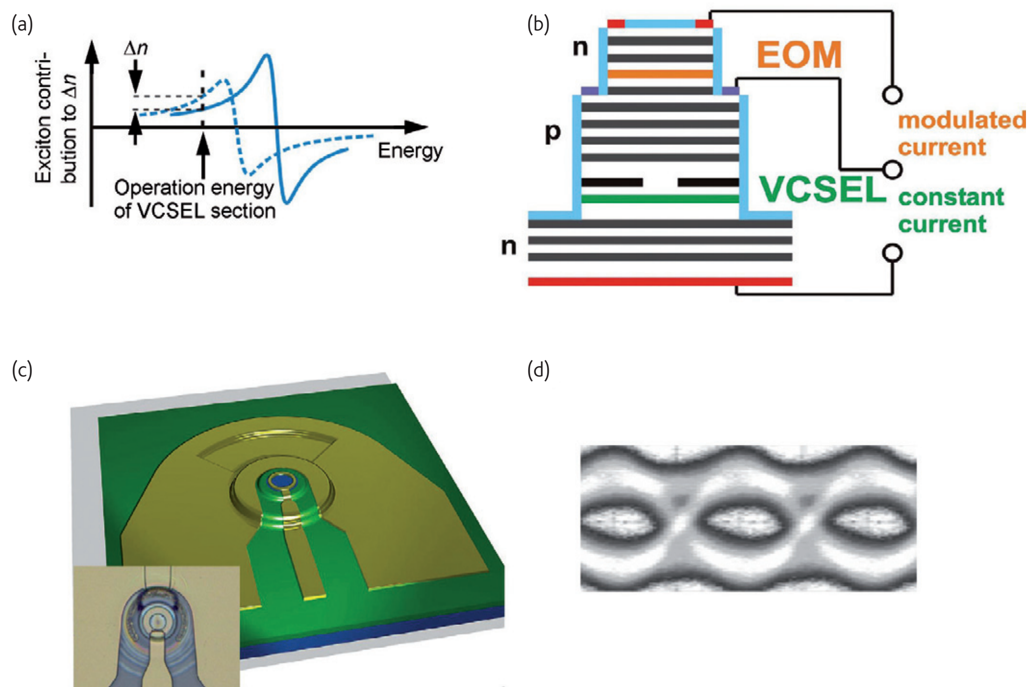

Fig. 5 Principle and proof-of-concept of a monolithic electro-optically modulated vertical-cavity surface-emitting laser (EOM-VCSEL). (a) Schematic of the electro-optic effect used for modulation. The refractive index changes by Δn at the operation wavelength of the device due to the field-induced energy shift of the exciton absorption. (b) Schematic of the EOM-VCSEL. The device consists of three DBR mirrors (black/white lines) which form two cavities: the VCSEL cavity operated in CW mode, and the EOM cavity which modulates the optical output of the VCSEL underneath. (c) Layout of an EOM-VCSEL prototype. (d) Eye diagram demonstrating 10 Gb/s operation of an EOM-VCSEL.

resonance of an exciton confined in a quantum well induced by an electric field (Fig. 5a). This effect was previously employed to modulate the internal loss by a voltage-controlled QW absorber in the upper mirror of a VCSEL[43]. Recent work stresses that the use of refractive-index modulation is much more efficient[44,45]. Furthermore, if the voltage-controlled modulator is placed in a resonantly coupled cavity, the modulation of the light output is predominantly governed by the electro-refractive effect rather than by electroabsorption[46]. Fig. 5a illustrates that the refractive index is changed by Δn at an operation wavelength beneath the exciton resonance. This effect is employed in a coupled-cavity device to change the transmittance of the modulator section avoiding significant slow absorption processes. The design of the device with a VCSEL section operated in CW mode and a reverse-biased modulator section is shown in Fig. 5b. The layout of such an EOM-VCSEL given in Fig. 5c shows the broad top *n* contact and the narrow central *p* contact of the modulator section. The open eye of the 10 Gb/s data stream of an EOM-VCSEL grown by MOCVD is shown in Fig. 5d[47]. The device exhibited temperature-stable operation at 845 nm up to 85 °C with low power consumption. EOM-VCSELs emitting at 960 nm grown using MBE achieved 60 GHz electrical bandwidth and an optical bandwith larger than 35 GHz[48].

Micro/nanolasers with metal-coated cavity

Recent breakthroughs sparked interest for semiconductor plasmonic nanolasers on Si for applications in future optical interconnects. Semiconductor lasers with a metal-coated cavity have advantages such as stronger optical confinement and smaller device size not achievable with dielectric structures, excellent isolation from crosstalk in device arrays, and excellent thermal conduction for heat removal. Recent progress lead to the demonstration of room temperature operation in pulsed mode[48] and, shortly after, CW operation[49]. Metal-assisted optical field confinement allows squeezing of visible light to a few nanometers[50]. The effect of the metal coating on the effective refractive index is illustrated in Fig. 6a for a coaxial core-shell structure basically representing the pillar structure of a vertical-emitting laser[51]. Due to the negative permittivity of the metal shell the modal effective index of the structure decreases strongly as the core diameter becomes smaller. Knowledge of the size-dependent optical properties allows the design of an efficient resonant structure with optical feedback for room-temperature CW operation as shown in Fig. 6b[52]. The active region (here MQWs) are clad by a lower Ag mirror and an upper DBR mirror, where light is coupled out. The simulation in Fig. 6b shows that the optical field in the cavity has the profile of the fundamental HE_{11} mode and yields a *Q* factor of 556. The calculated amplified spontaneous emission is given in Fig. 6c for varying surface-carrier density per QW. The simulations are well confirmed by the experimental realization of the device[49], yielding a *Q* factor of 580 near threshold and a total power in the μW range. The small thermally induced red shift in the experimental spectra of Fig. 6c indicates a very

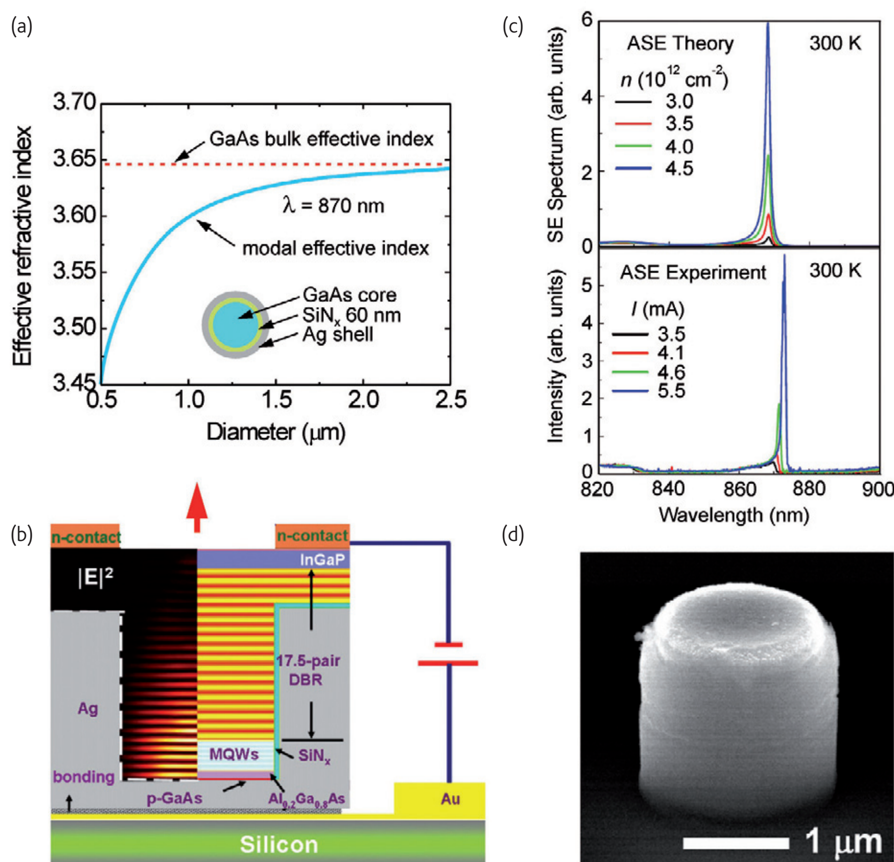

Fig. 6 A metal-cavity surface-emitting microlaser. (a) Modal effective index of a structure with semiconductor core/isolator/metal as a function of the core diameter. (b) Schematic of a microlaser with bottom Ag mirror and top DBR mirror. Left half: simulated optical field pattern $|E|^2$*, right half: layer structure. (c) Calculated and experimental amplified-spontaneous-emission (ASE) spectra. Theoretical and experimental parameters signify values of assumed surface carrier-density and injection current, respectively (d) Scanning electron micrograph of the device structure, encapsulated by a thin* SiN_x *isolator, before metal coating.*

low thermal impedance of the device, yielding a record-low value of 1.237 °C/mW for a device of 2 μm in diameter and 2.5 μm in length.

Devices addressing individual quantum dots

Individually addressed quantum dots are the subject of a particularly active field of current research. Single-QD devices are compact and easy to integrate into existing technology, making them attractive for applications in quantum information processing and quantum cryptography. A key element for quantum computing, the quantum memory, was successfully demonstrated using the storage of the polarization state of a single photon in a single QD[54,55]. We will focus on the key element of quantum communication, the single-photon emitter. Such an emitter must be able to emit just a single photon on demand. An alternative scheme is based on an emitter which emits exactly one pair of entangled photons. Both tasks can be accomplished using single quantum dots. Devices with individually addressed single QDs can provide deterministic integrated light sources providing non-classical emission characteristics, enabling secure bit-pattern transmission for quantum communication.

Single-photon source

Major steps in the realization of such a deterministic light source have recently been accomplished, such as *pin* diode structures with a low-density QD layer and spatial filtering using a metal aperture[56], or spectral filtering by a micropillar cavity with small mode volume[57]. A breakthrough was the demonstration of selective electrical injection into a single QD[58,59,60]. Individual addressing of just a single dot is achieved by confining the current path in a *pin* diode structure to the location of a single dot as illustrated in Fig. 7a. The task was realized by using an oxide aperture with a small opening in close proximity to the dot. The micrograph given in Fig. 7b depicts the small AlO_x aperture located 20 nm above the InAs QD layer[58]. The electroluminescence of this device shows a single emission line originating from this quantum dot (Fig. 7c). From the saturation of the luminescence at 1 nA (corresponding to 5 electrons per ns) and the typical exciton lifetime of 1 ns an injection efficiency of 20 % in this simple device is concluded[61]. The emission is enhanced and directed into a distinctive mode by placing the QD into a cavity clad by Bragg reflectors. Using such a resonant-cavity (RC)-LED design, the luminescence intensity

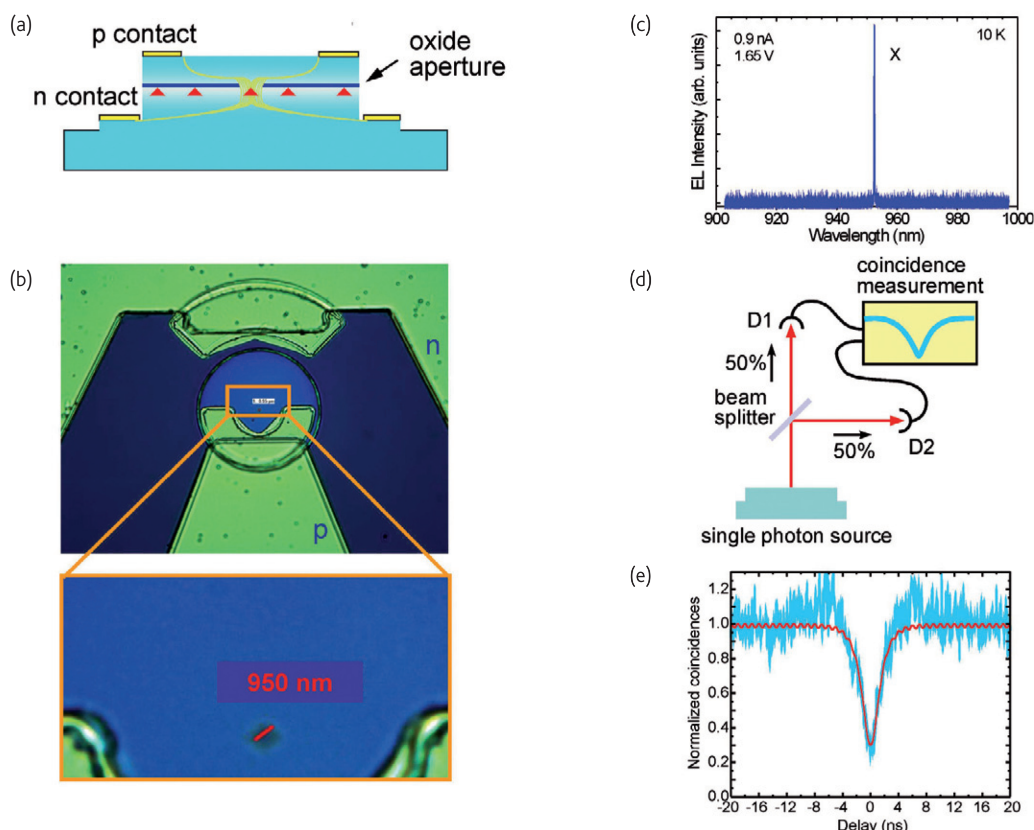

Fig. 7 A semiconductor single-photon source. (a) Schematic view in cross section. The oxide aperture confines the current path (light green) in the mesa structure to the excitation of a single quantum dot (red). (b) Top view of the device showing the small aperture and the contacts. (c) Emission spectrum of the device. Only the exciton emission of a single quantum dot is observed at low injection current. (d) Experimental setup with two single-photon detectors D1, D2 for measuring the correlation of the emitted photons. (e) Measured (black curve) and simulated coincidences of photons arriving at the two detectors versus the delay of the arrival time. Since no photon can be detected simultaneously at both detectors from a true single-photon source, the coincidences drop at 0 delay. The red curve is a simulation of a perfect single-photon source, taking the limited time resolution of the setup into account.

was increased by a factor of 20 due to the increased spontaneous emission rate and out-coupling efficiency[62]. The single-photon nature of the emission is revealed by a photon-correlation measurement using a Hanbury-Brown-Twiss (HBT) setup. The setup illustrated in Fig. 7d measures the autocorrelation of the photons emitted from the source by splitting the emission into two beams. In a single-photon event the sensitive detectors D1 and D2 can not simultaneously receive a signal. Consequently the number of signal coincidences at D1 and D2 is expected to drop to 0 at zero time delay. The actual decrease to 20 % shown in Fig. 7e is due to the limited time resolution of the setup[62]. The red, simulated curve in the figure gives the response of a perfect single-photon device pulsed at 1 GHz repetition rate. The excellent agreement with the measured correlation proved single-photon emission and the high-speed capability of the single-photon device.

Source of entangled photon pairs

The preparation of entangled photon pairs extends the options for quantum information and quantum logic operations. Entangled photons may be emitted from a quantum dot loaded with a biexciton, i.e., with two electrons and two holes: the radiative decay of one exciton followed by that of the other generates two photons. These photons are polarization entangled, if the exciton state is not split. While a fine-structure splitting occurs in dots of reduced symmetry (yielding only classically correlated photon pairs), negligible splitting is expected for high-symmetry InAs QDs grown on (111) oriented GaAs substrates[63]. QDs were realized on (111) GaAs by different approaches[64,65] and shown to allow for single-photon operation[65]; weak symmetry breaking has been observed so far. Recent success in the demonstration of entangled photon pairs is based on careful preselection of QDs grown on (001) GaAs[66,67] and a promising high entanglement fidelity of up to 0.82 was achieved in an electrically driven device[67].

Devices addressing small ensembles of quantum dots

QD flash memory

Besides the optical applications pointed out above, QDs are also attractive for data storage. Two different semiconductor memories

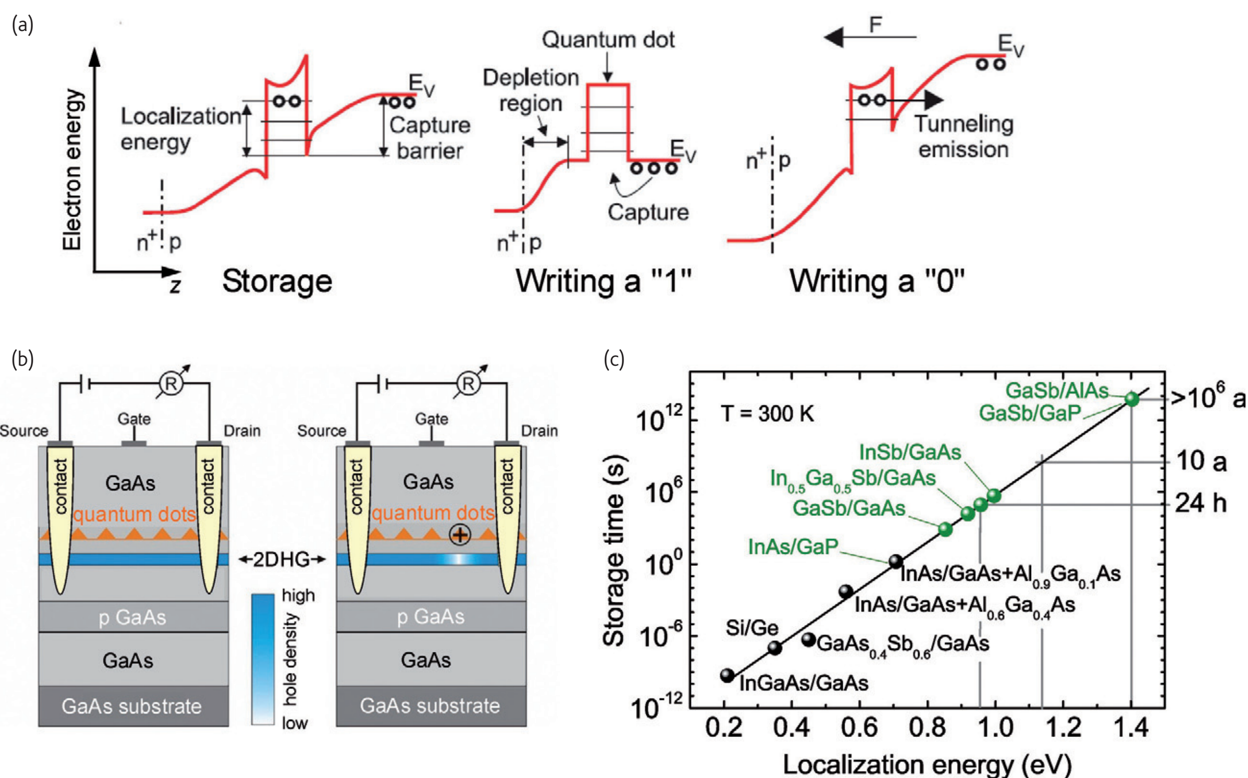

Fig. 8 Prototype of a quantum-dot flash memory. (a) Operation principle of storage, writing, and erasing. Left: binary states 0 and 1 are represented by a QD being filled with holes or being empty, respectively. The diagram shows two holes confined in a QD. Middle: writing of a 1 by applying a bias which eliminates the capture barrier. Right: Erasing the memory by applying a high electric field which extracts the charge from the QD. (b) Schematic of the layer structure. The device is a p-MODFET with a two-dimensional hole gas (2DHG) for reading the charge state of the QD. Stored charges locally deplete the 2DHG and increase the detected source-drain resistance. (c) The hole storage-time depends on the localization energy. The diagram shows experimental data (black circles) and predicted storage time for various QD/matrix materials, the solid line is a fit to experimental data.

dominate today's devices. First the dynamic random-access memory (DRAM) with a fast access time (< 20 ns) and a good endurance (> 10^{15} write/erase cycles), but a poor retention time (~10 ms) requiring energy-consuming refresh cycles. Second the flash memory with a long retention time (10 years), but a poor write time (~µs) and endurance (< 10^6). All existing charge-based memories feature this trade-off between long retention times and fast write/erase cycles. Memories based on QDs are an interesting option to resolve the trade-off and fabricate non-volatile memories with fast read/write operations and good endurance. The basic idea is to replace the fixed barriers for charge storage (like the Si/SiO_2 barrier) by an engineered variable band structure. The example illustrated in Fig. 8a employs the storage of holes in a quantum dot[68]. The depicted barriers given by the valence-band discontinuities of the QD/matrix interface can be altered by applying a bias voltage in the device. Thereby writing and erasing cycles can be performed as indicated in the figure. Read-out of the stored information is made by measuring the conductance of a two-dimensional hole gas (2DHG) placed underneath the dot layer (Fig. 7b): stored carriers reduce the charge density and the mobility in the 2DHG and hence the conductance.

The write time in the present concept is controlled by the carrier relaxation from the band edge to the QD states, which is below picoseconds at room temperature[69,70]. In the first prototypes a write time of 80 ns was achieved, limited by a low parasitic cut-off frequency but already close to present DRAM data[71]. The storage time scales with the localization energy of the confined carriers and

Instrument citation

Rhode & Schwarz electrical spectrum analyzer
Ando optical spectrum analyzer
HP network analyzer
HP LCR meter
Agilent oscilloscope
SHF bit pattern generator
APE autocorrelator
Perkin Elmer Si APDs
Acton triple monochromator
Boonton capacitance bridge

hence depends on the QD/matrix materials. Fig. 8c show achievements accomplished so far, along with predicted data for materials presently under investigation by us[72]. An increase of the localization energy from 210 meV in InAs/GaAs QDs to 710 meV by inserting an $Al_{0.9}Ga_{0.1}As$ barrier underneath the QDs pushed the hole storage-time from 0.5 ns[73] to 1.6 s[72], i.e., already to 10^3 times the typical DRAM refresh time. Predictions drawn in Fig. 8c are based on 8-band kp calculations, yielding a localization as large as 1.4 eV for GaSb/AlAs QDs, translating to an average hole storage time beyond 10^6 years. The present data demonstrate the feasibility of a QD-based memory and the accomplished fast progress, making such a concept an interesting option for future fast flash-memory devices.

Conclusion

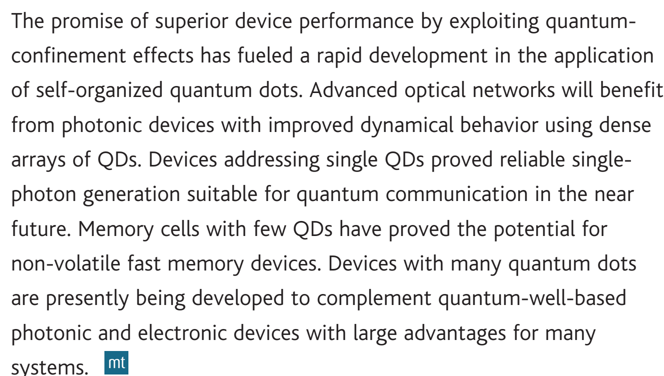

The promise of superior device performance by exploiting quantum-confinement effects has fueled a rapid development in the application of self-organized quantum dots. Advanced optical networks will benefit from photonic devices with improved dynamical behavior using dense arrays of QDs. Devices addressing single QDs proved reliable single-photon generation suitable for quantum communication in the near future. Memory cells with few QDs have proved the potential for non-volatile fast memory devices. Devices with many quantum dots are presently being developed to complement quantum-well-based photonic and electronic devices with large advantages for many systems. mt

REFERENCES

1 Bimberg, D., Grundmann, M., and Ledentsov, *N. N., Quantum Dot Heterostructures*, Wiley, Chichester, (1999).

2 Dingle, R., and Henry, C. H., *U. S. Patent* 3,982,207 (1976).

3 Asada, M., *et al.*, *J Quantum Electron* (1986) **QE-22**, 1915.

4 Arakawa, Y., and Sakaki, H., *Appl Phys Lett* (1982) **40**, 939.

5 Kirstaedter, N., *et al.*, *Electron Lett* (1994) **30**, 1416.

6 Ledentsov, N. N., *et al.*, *IEEE J Sel Topics Quantum Electron* (2000) **6**, 439.

7 Zia Laser Inc., Albuquerque, NM, USA; NL Nanosemiconductors/Innolume GmbH, Dortmund, Germany.

8 Grundmann, M., *Physica E* (2000) **5**, 167.

9 Luque, A., *et al.*, *Phys Rev Lett* (1997) **78**, 5014.

10 Popescu, V., *et al.*, *Phys Rev B* (2008) **78**, 205321.

11 Hubbard, S. M., *et al.*, *Appl Phys Lett* (2008) **92**, 123512.

12 Kirstaedter, N., *et al.*, *Appl Phys Lett* (1996) **69**, 1226.

13 Ribbat, C., *et al.*, *Appl Phys Lett* (2003) **82**, 952.

14 Gehrig, E., *et al.*, *Appl Phys Lett* (2004) **84**, 1650.

15 Ribbat, C., *et al.*, *Electron Lett* (2001) **37**, 174.

16 Huyet, G., *et al.*, *Phys Stat Sol A* (2004) **201**, 345.

17 Borri, P., *et al.*, *IEEE Photonics Technol Lett* (2000) **12**, 594.

18 Borri, P., *et al.*, *J Opt A: Pure Appl Opt* (2006) **8**, S33.

19 Williams, K. A., *et al.*, *New J Phys* (2004) **6**, 179.

20 Bimberg, D., *et al.*, *Phys Stat Sol A* (2006) **203**, 3523.

21 Kuntz, M., *et al.*, *IEEE Proc* (2007) **95**, 1767.

22 ITU Recommendation 2001, *The control of jitter and wander within the optical transport network (OTN)*, Recommendation G.8251, ITU-T.

23 Schmeckebier, H., *et al.*, *Opt Express* (2010) **18**, 3415.

24 Meuer, C., *et al.*, *IEEE J Sel Topics in Quantum Electron* (2009) **15**, 749.

25 Joergenson, C., *et al.*, *IEEE J Sel Topics in Quantum Electron* (1997) **3**, 1168.

26 Kim, J., *et al.*, *J Quantum Electron* (2009) **45**, 240.

27 Vallaitis, T., *Opt Express* (2008) **16**, 170.

28 Schmeckebier, H., *et al.*, *Semicond Sci Technol* (2011) **26**, 014009.

29 Meuer, M., *et al.*, *Opt Express* (2011) **19**, 5134.

30 Contestabile, G., *et al.*, *J Quantum Electron* (2010) **46**, 1696.

31 A. Mutig *et al.*, *Appl Phys Lett* (2009) **95**, 131101.

32 Westbergh, P., *et al.*, *Electron Lett* (2010) **46**, 1014.

33 Hofmann, W., *et al.*, Paper PDPC5 presented at OFC/NFOEC Conferences, Los Angeles, CA, 2011.

34 Saito, H., *et al.*, *Appl Phys Lett* (1996) **69**, 3140.

35 Schur, R., *et al.*, *Jpn J Appl Phys* (1997) **35**, L357.

36 Lott, J. A., *et al.*, *Electron Lett* (1997) **33**, 1150.

37 Hopfer, F., *et al.*, *Appl Phys Lett* (2006) **89**, 061105.

38 Hopfer, F., *et al.*, *IEEE J Sel Topics Quantum Electron* (2007) **13**, 1302.

39 Lenz, A., *et al.*, *Appl Phys Express* (2010) **3**, 105602.

40 Mutig, A., *et al.*, *Electron Lett* (2008) **44**, 1305.

41 Miller, D. A. B., *et al.*, *Phys Rev B* (1985) **32**, 1043.

42 Hudgings, J. A., *et al.*, *Appl Phys Lett* (1998) **73**, 1796.

43 Ledentsov, N. N., *et al.*, *Proc IEEE* (2007) **95**, 1741.

44 Ledentsov, N. N., *et al.*, *U. S. Patent* 7,369,583 B2 (2008).

45 Shchukin, V. A., *et al.*, *Proc SPIE* (2008) **OH1**, 6889.

46 Germann, T., *et al.*, *Phys Stat Sol C* (2010) **7**, 2552.

47 Paraskevolpoulos, A., *et al.*, Paper PDP22 presented at OFC/NFOEC Conferences, Anaheim, CA, 2006.

48 Hill, M. T., *et al.*, *Opt Express* (2009) **17**, 11107.

49 Lu, C.-Y., *et al.*, *Appl Phys Lett* (2010) **96**, 251101.

50 Miyazaki, H. T., *et al.*, *Phys Rev Lett* (2006) **96**, 097401.

51 Lu, C.-Y., *et al.*, *Semicond Sci Technol* (2011) **26**, 014012.

52 Chang, S.-W., *et al.*, *IEEE J Sel Topics Quantum Electron* (2011) **17**, in press.

53 Lu, C.-Y., *et al.*, *Photon Technol Lett* (2011) **23**, 1031.

54 Young, R. J., *et al.*, *New J Phys* (2007) **9**, 365.

55 Heiss, D., *Phys Rev B* (2008) **77**, 235442.

56 Yuan, Z., *et al.*, *Science* (2002) **295**, 102.

57 Heindl, T., *et al.*, *Appl Phys Lett* (2010) **96**, 011107.

58 Lochmann, A., *et al.*, *Electron Lett* (2006) **42**, 774.

59 Monat, C., *et al.*, *Nano Lett* (2006) **6**, 1464.

60 Ellis, D. J. P., *et al.*, *Appl Phys Lett* (2006) **88**, 133509.

61 Scholz, M., *et al.*, *Opt Express* (2007) **15**, 9107.

62 Stock, E., *et al.*, *Semicond Sci Technol* (2011) **26**, 014003.

63 Schliwa, A., *et al.*, *Phys Rev B* (2009) **80**, 161307(R).

64 Karlsson, K. F., *Phys Rev B* (2010) **81**, 161307 (R).

65 Stock, E., *et al.*, *Appl Phys Lett* (2010) **96**, 093112.

66 Hafenbrak, R., *et al.*, *New J Phys* (2007) **9**, 315.

67 Salter, C. L., *et al.*, *Nature* (2010) **465**, 594.

68 Geller, M., *J Phys: Condens Matter* (2008) **20**, 454202.

69 Müller, T., *Appl Phys Lett* (2003) **83**, 3572.

70 Geller, M., *Appl Phys Lett* (2006) **89**, 232105.

71 Marent, A., *Appl Phys Lett* (2009) **95**, 242114.

72 Marent, A., *Appl Phys Lett* (2007) **91**, 242109.

73 Geller, M., *Phys Rev B* (2006) **73**, 205331.